Optimization of element length for imaging small volumetric reflectors with linear ultrasonic arrays

T. S. Barber, P. D. Wilcox, and A. D. Nixon

Citation: AIP Conference Proceedings **1706**, 020016 (2016); doi: 10.1063/1.4940462
View online: http://dx.doi.org/10.1063/1.4940462
View Table of Contents: http://scitation.aip.org/content/aip/proceeding/aipcp/1706?ver=pdfcov
Published by the AIP Publishing

Optimization of Element Length for Imaging Small Volumetric Reflectors with Linear Ultrasonic Arrays

T. S. Barber[1, 2, a)], P. D. Wilcox[1)] and A. D. Nixon[2)]

[1]*University of Bristol, Mechanical Engineering, Queens Building, University Walk, Bristol, BS8 1TR, United Kingdom*

[2]*BAE Systems Submarines, Materials Technology, Barrow-in-Furness, Cumbria, LA14 1AF, United Kingdom*

[a)] Corresponding author: T.S.Barber@bristol.ac.uk

Abstract. A 3D ultrasonic simulation study is presented, aimed at understanding the effect of element length for imaging small volumetric flaws with linear arrays in ultrasonically noisy materials. The geometry of a linear array can be described by the width, pitch and total number of the elements along with the length perpendicular to imaging plane. This paper is concerned with the latter parameter, which tends to be ignored in array optimization studies and is often chosen arbitrarily for industrial array inspections. A 3D analytical model based on imaging a point target is described, validated and used to make calculations of relative Signal-to-Noise Ratio (SNR) as a function of element length. SNR is found to be highly sensitive to element length with a 12dB variation observed over the length range investigated. It is then demonstrated that the optimal length can be predicted directly from the Point Spread Function (PSF) of the imaging system as well as the natural focal point of the array element from 2D beam profiles perpendicular to the imaging plane. This result suggests that the optimal length for any imaging position can be predicted without the need for a full 3D model and is independent of element pitch and the number of elements. Array element design guidelines are then described with respect to wavelength and extensions of these results are discussed for application to realistically-sized defects and coarse-grained materials.

INTRODUCTION

Linear ultrasonic arrays are used across many engineering sectors to perform bulk NDE inspection of safety-critical components. Phased Array (PA) inspection techniques utilize the independent transducer elements of arrays to steer ultrasonic energy; this results in enhanced flaw detection and improved characterization capability when compared with single element transducers. Focused 2D ultrasonic images are obtained from the phased transmission of the array elements or alternatively by post processing of the Full Matrix Capture (FMC) signals acquired from each transmitter and receiver combination in the array [1-2]. Linear arrays can be defined by the width, W, length, L, and pitch, P of the elements, as described in Fig. 1 along with the total number of elements and the typical frequency characteristics of the ultrasonic pulse. In industry, the choice of these parameters for a particular inspection depends on thickness of the sample, the required imaging resolution and the microstructure of the material. Well proven "rules of thumb" exist for defining most of these parameters based on the wavelength of the ultrasound and the type of flaw required to be detected, yet the element length, L, is often chosen arbitrarily. In the literature, many authors have engaged in parametric studies to optimize array imaging performance but generally the out-of-plane element length is ignored [3-5]. This can be attributed to the common assumptions made about scatterer behavior and the element width to length ratio (which are typically defined so that there is little variation in the ultrasonic field perpendicular to the imaging plane). With these simplifications, a 2D approximation to the ultrasonics in the imaging plane can be applied to simplify analysis and reduce computational load for intensive modelling studies.

42nd Annual Review of Progress in Quantitative Nondestructive Evaluation
AIP Conf. Proc. 1706, 020016-1–020016-10; doi: 10.1063/1.4940462

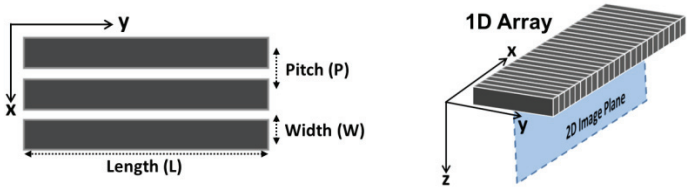

FIGURE 1. Schematic describing the key geometrical parameters of linear ultrasonic array elements. The transmission signal center frequency, bandwidth and the number of elements fully define the array. 2D image is formed by focusing in the *XZ* plane.

This work aims to quantitatively understand the effect of element length on the detectability of small volumetric flaws in inherently noisy materials where commonly used 2D approximations cannot be applied. In the context of this paper small volumetric flaws are defined as defects that scatter ultrasound in a similar way to a point target (e.g gas pores, inclusions and tip signals from short through-wall cracks). Industrial interest in the application of ultrasonic arrays to volumetric defects has increased more recently as NDE groups attempt to replace traditional radiographic inspection with safer and cheaper ultrasonic techniques. Radiography is naturally better suited to detecting some volumetric defects and so a key practical objective of this work is to identify guidelines to optimize array design to improve the probability of detection of volumetric flaws in ultrasonically-noisy materials.

In this paper, a 3D frequency-domain analytical model is used to understand the problem and is described in the next section along with a general description of the imaging process and the assumptions made in the simulation of microstructural grain noise. Experimental validation of the noise assumptions is presented in the following section along with the results and conclusions from the modelling work.

THEORY

3D Model of Full Matrix Capture Data

In a homogenous and isotropic half space, the FMC signals, $F_{ij}(\boldsymbol{q}; \omega)$, obtained from an array with an element frequency response $F_0(\omega)$, element center positions $\boldsymbol{u_i}$, with a target reflector located at a point $\boldsymbol{q}$ can be represented as:

$$F_{ij}(\boldsymbol{q};\omega) = F_0(\omega)\, D(\hat{\boldsymbol{x}}_i;\omega) D(\hat{\boldsymbol{x}}_j;\omega)\, (|\,\boldsymbol{x}_i\,||\,\boldsymbol{x}_j\,|)^{-\beta} T(|\,\boldsymbol{x}_i\,|,|\,\boldsymbol{x}_j\,|;\omega) S(\hat{\boldsymbol{x}}_i, \hat{\boldsymbol{x}}_j;\omega) \tag{1}$$

where the distance from an element centered at $\boldsymbol{u_i}$ to the target is $\boldsymbol{x_i}=\boldsymbol{q}-\boldsymbol{u_i}$ and $D(\hat{\boldsymbol{x}}_{i,j}\,;\,\omega)$ represents the angular sensitivity or "directivity" of the array elements in transmission and reception respectively. The fourth term in (1) represents beam spread ($\beta = 0.5$ for 2D cylindrical wave model and $\beta = 1$ for 3D spherical waves) and the functions $T(|\,\boldsymbol{x_i}\,|,|\,\boldsymbol{x_i}\,|;\omega)$ and $S(\hat{\boldsymbol{x}}_i,\ \hat{\boldsymbol{x}}_j\,;\,\omega)$ describe the signal propagation and scattering properties of the target.

The model described by (1) is desirable to use owing to its computational efficiency but is only suitable for target positions located in the far-field of all the elements where directivity and beam spread can be described by separate functions. This condition is related to the element dimensions and the ultrasonic wavelength and can be loosely by represented as $|\,\boldsymbol{x_i}\,| > \max(W^2, L^2)/4\lambda$ in 3D or $|\,\boldsymbol{x_i}\,| > W^2/4\lambda$ in a 2D approximation. For linear arrays the statement for the 2D model is valid as W is usually sub-wavelength yet for a 3D model common values of L are of the order of tens of wavelengths and are comparable to target distances in the component. Numerical Finite Element (FE) modelling could be used as an alternative but in 3D this is computationally intensive and time consuming especially when being used for multi-parameter studies. An alternative approach is to split the area of each of the N elements, $\boldsymbol{\phi_n}$, into S equally sized sub-elements which can be defined by the sub-element center position vectors $[\boldsymbol{v_1} \ldots \boldsymbol{v_{NS}}]$. The dimensions of the sub-elements (and hence S) are chosen to satisfy the far-field approximations so that the frequency-domain analytical model in (1) can be used. FMC signals for each transmit receive element combination, $F_{ij}(\boldsymbol{q}; \omega)$, can then be obtained by selective summation of the modelled sub-element FMC data set, $G_{kl}(\boldsymbol{q}; \omega)$ simulated using (1):

$$F_{ij}(\boldsymbol{q};\omega) = \sum\nolimits_{k,l} G_{kl}(\boldsymbol{q};\omega) H_k(\boldsymbol{\varphi_i}) H_l(\boldsymbol{\varphi_j}) \tag{2}$$

where $H_s(\phi_n)$ are a set of binary coefficients with the value $H_s(\phi_n)$=1 if the sub-element indices s refers to a sub-element that is part of the element n and is 0 otherwise.

Point Spread Function

In a linear ultrasonic system, an FMC "frame" is the maximum amount of independent data that can be obtained from an array and is a basis from which all other array data or focused images can be derived through post processing. An image amplitude $I(\boldsymbol{r})$ obtained from an image point $\boldsymbol{r}$ from FMC data $F_{ij}(\omega)$ can be generally described in frequency-domain form as:

$$I(\boldsymbol{r}) = \left| \int \sum_{i=1}^{N} \sum_{j=1}^{N} F_{ij}(\omega) A_{ij}(\omega; \boldsymbol{r}) d\omega \right| \tag{3}$$

where $A_{ij}(\omega; \boldsymbol{r})$ is a complex coefficient that describes the imaging algorithm operating on the FMC data including phase delays, amplitude weighting coefficients and any other signal processing operations. For a linear array (which can only focus in a 2D image plane below the array) the coefficients $A_{ij}(\omega; \boldsymbol{r})$ are independent of element length. In this paper, element length (L) is the array parameter of interest and the others are kept constant so that the coefficients $A_{ij}(\omega; \boldsymbol{r})$ that define the imaging algorithm are fixed. In this work, the 2D Total Focusing Method (TFM) imaging algorithm is used as it is simple to apply, robust, and has demonstrated a significant improvement in imaging performance compared to conventional B-Scans or Sector-Scan phased array techniques [1].

A useful concept to measure the combined array and imaging algorithm performance (particularly for imaging volumetric flaws) is the Point Spread Function (PSF). The PSF, $P(\boldsymbol{r} \mid \boldsymbol{q})$ (where the notation "|" implies "given") is the image $I(\boldsymbol{r})$ obtained from a single, frequency independent, omni-directional point target at $\boldsymbol{q}$. Metrics such as the peak PSF amplitude and the area of the PSF can be used to compare the performance of array and imaging algorithm combinations. The PSF can be interpreted as a subset or section of a wider 5 dimensional function $P(\boldsymbol{r}, \boldsymbol{q})$ that fully describes the focusing capability of the system across the imaging space $\boldsymbol{r}$ and target space $\boldsymbol{q}$.

Microstructural Noise Model

The theory described in the previous sections has focused on modelling and imaging the response from a single target of interest in an environment free from any other signals but in practice an ultrasonic measurement through a material is subject to both random and coherent noise. For industrial NDT applications, the main limitation to array performance is coherent noise or "backscatter" from the material microstructure. This cannot be temporally averaged out (unlike random noise), and so it is important than an optimization study is able to model and account for its effect on imaging performance. This research area has been particularly active in recent years with detailed FE Models and first principles studies modelling and describing scattering from individual and distributions of grains in materials and welds [4, 6]. Generally these approaches are computationally expensive and impractical particularly when applied to a 3D array inspection optimization problem. For the purposes of this work a relatively simple analytical model of noise is used based on four assumptions:

- Single scattering – Noise is dominated by contributions from ray-paths that leave the array, scatter off a single grain and return to the array without any other interaction.
- Each grain behaves as an omni-directional frequency independent point scatterer.
- The only random variable associated with scattering from each position is a zero mean complex amplitude factor.
- There is no spatial correlation between material scattering from different positions regardless of how close they are.

Considering these assumptions, an equation for the expected Signal-to-Noise Ratio, $SNR(\omega; \boldsymbol{r})$, from a given array can be defined, represented as a superposition of the PSF's from each grain in the material volume [7]

$$SNR(\omega; \boldsymbol{r}) = \frac{\rho(\omega) \mid P(\boldsymbol{r} \mid \boldsymbol{q} = \boldsymbol{r}) \mid}{\sigma(\omega)\sqrt{\int \mid P(\boldsymbol{r} \mid \boldsymbol{q}) \mid^2 d\boldsymbol{q}}} = \Delta(\omega)\ \Gamma(\omega; r) \tag{4}$$

where the numerator describes the "signal" component at an image point $\boldsymbol{r}$ which in this case is that of a point target (a useful approximation for small volumetric flaws) and $\rho(\omega)$ is a material property that describes the amplitude of the signal in the absence of noise. The denominator represents the noise component with the term in the square root essentially an integration of the PSF's from all grains and $\sigma(\omega)$ a material dependent variable describing the backscatter amplitude as a function of frequency. This equation demonstrated encouraging results when imaging inherently noisy copper at 5MHz predicting the correct SNR improvement with array aperture size and is therefore considered an appropriate model to use for this study [7].

It is instructive to split (4) into a component that is entirely dependent on material and grain structure properties, $\Delta(\omega) = \rho(\omega)/\sigma(\omega)$, and a second component $\Gamma(\omega; \boldsymbol{r})$ that contains a dependence on the geometrical parameters of the array, imaging algorithm and defect or "signal". In this paper, $\Delta(\omega)$ is fixed throughout implying that the probe frequency characteristics are constant and material is not changed (probe frequency should be chosen first based thickness, required resolution and material grain structure). This reduces the overall element length optimization problem to a maximization over the objective function, $\Gamma(\omega; \boldsymbol{r})$:

$$L_{Opt}(\boldsymbol{r}) \sim \arg\max_{L}(\Gamma(\omega; r)) \tag{5}$$

With the assumptions outlined in this model the maximization is dependent only the geometrical parameters of both the array and the position of the target relative to the ultrasonic wavelength. Consequently, $\Gamma(\omega; \boldsymbol{r})$ is a function of a normalized frequency spectrum $\omega_n = \omega/\omega_c$ where ω_c is the physical center frequency of the probe. For generality, results and geometrical parameters presented throughout this paper will therefore be presented in terms of wavelength, λ, at the probe center frequency.

RESULTS

Experimental Validation of Noise Model

Given the considerable simplifications made in the described coherent noise model it is essential to demonstrate some form of validation. The experimental noise data for the three different element lengths were synthesized by using a 15MHz 1.5D array (Fig. 2(a)) which consists of three rows of 84 elements of length R perpendicular the imaging plane [8]. The spacing between the rows of the array in this dimension are negligible (<λ/5). Therefore, FMC data for 1D arrays with element lengths of $L = R$, $2R$ or $3R$ can be synthesized from experimentally-obtained FMC array from the 1.5D array by selective summations of appropriate signals. This approach negates the requirement of multiple probes with different element lengths whilst ensuring the probe input signal, pitch and number of elements is identical for each length. The experimental noise was measured using images (Fig. 2(b)) from 20 FMC frames obtained from different positions in the material; the noise images can be considered as statistically independent and the Root Mean Square (RMS) noise level at each depth can be estimated. Figure 2(c) shows a comparison of experimentally-measured microstructural noise and modelled noise as a function of depth in direct contact TFM images for three different element lengths, L, in defect-free stainless steel plate. The simulated noise results were obtained from the model described in the previous section and numerically calculated from the denominator in (4). From Fig. 2(c) an encouraging agreement is evident with a notable but not significant variability between noise measurements. This can be explained from the limited number of independent sets data that were collected which ultimately results in a less accurate estimation to the RMS noise level at each depth.

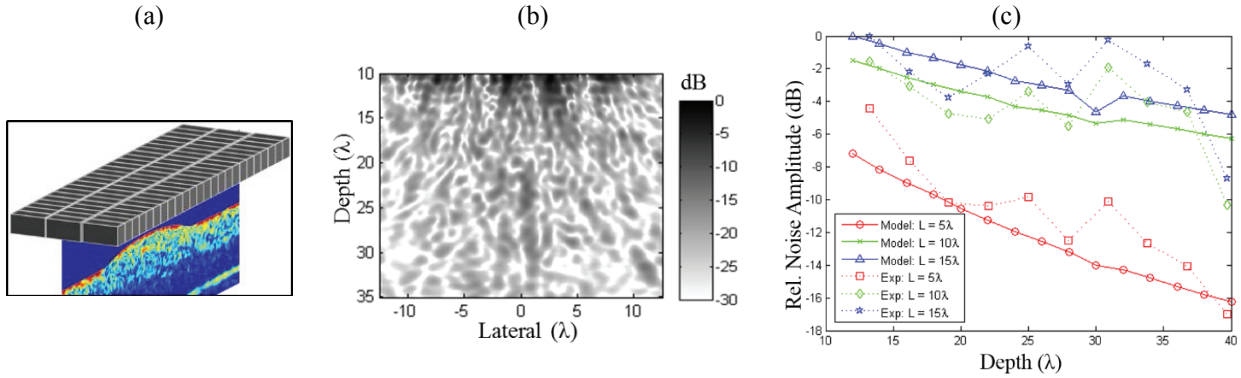

FIGURE 2. Experimental validation of microstructural noise model. (a) Schematic of 1.5D array used to synthesize different element lengths experimentally from one array (b) Example image of experimental microstructural noise. (c) Measured and simulated image noise level as a function of depth (normalized to wavelength at probe center frequency) in stainless steel for three arrays with different element lengths of 5λ, 10λ and 15λ but with all other array parameters identical. Experimental and simulated results are normalized separately.

Modelling Results

Point Spread Function

At a fixed frequency it can be seen from (4) that the PSF, $P(\boldsymbol{r} \mid \boldsymbol{q})$, is the key metric of the proposed model that influences SNR. Firstly in terms of image noise amplitude (denominator in (4)), where the PSF's from all grains in the material volume are integrated at each imaging point but equally for the image signal amplitude (the numerator), where the PSF provides a useful approximation to the scattering behavior of a spherical volumetric defect (e.g gas pore). It is therefore instructive at the outset to consider the behavior of the PSF as a function of element length (L) illustrated in Fig. 3. Consider a target positioned at $[0, 0, z=10\lambda]$ and an array consisting of 30 elements of width $W=0.5\lambda$ where W represents the element width as in Fig. 1. Each element emits a normalized frequency spectrum with a fractional -20dB bandwidth of 100% and the inter-element spacing of the array is assumed negligible so that the pitch P is equal to W.

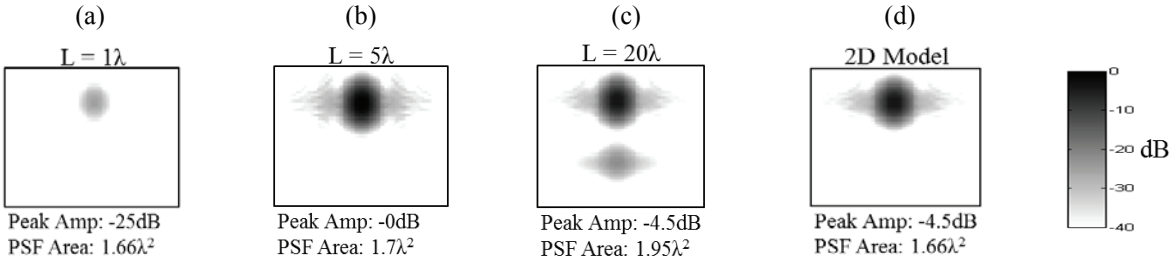

FIGURE 3. Example images of the Point Spread Function from a target at a depth of 10λ for L of: (a) 1λ, (b) 5λ, (c) 20λ and (d) a 2D Model without the effects of element length. The array is positioned above the images with the PSF Area and peak amplitude shown below.

In Fig. 3, a 25dB increase in absolute image amplitude (images are globally normalized) of the PSF is seen from $L=1\lambda$ to $L=5\lambda$ because of the increased active aperture of the element and the attendant reduction in beam spread. Note that this specific change in sensitivity will not necessarily be observed in the SNR as the reduced sensitivity of the aperture will also apply to grain noise as well as the target signal. At $L=20\lambda$ an additional "artefact" can be observed, approximately -20dB weaker than the main focus. This effect is analogous to grating lobes in array imaging and is initially identified when L reaches a critical length such that there is more than one path to the element aperture that the received wavefield will constructively sum. This is a direct result of using a finite size element aperture to image a point source field, with this secondary signal observed in the FMC data to occur later in time than the primary signal, hence causing an artefact at a larger depth than the true signal in a 2D image.

To analyze combined array and imaging algorithm performance two quantitative metrics are defined: (1) the PSF area, which is defined as the total area of the PSF image above a certain threshold relative to its peak amplitude and (2) the absolute value of the peak amplitude of the PSF. Both of these metrics are displayed for each image in Fig. 3 where a -20dB has been used as the threshold for the area calculation. The behavior of the two metrics is shown as a function of L in Fig. 4.

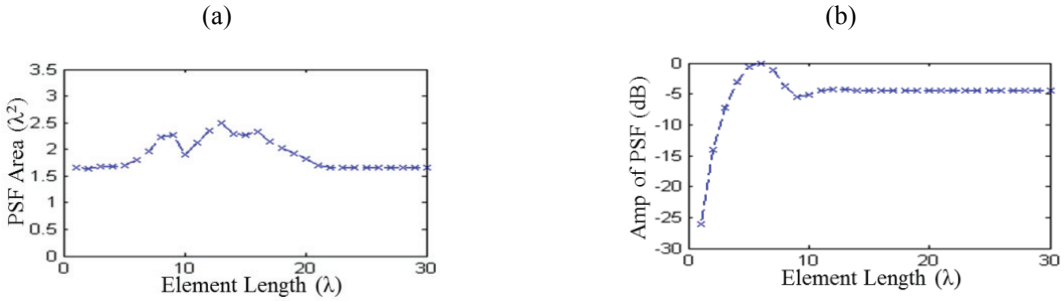

FIGURE 4. Point Spread Function characteristics as a function of L for a target at a depth of 10λ. (a) PSF area evaluated for a -20dB threshold and (b) PSF peak amplitude.

The PSF area remains constant until the second "artefact" signal occurs beyond $L=5\lambda$ in the images, it then increases before returning to a constant value once the artefact is below the -20dB threshold. In contrast, the PSF amplitude increases and clearly peaks, at $L=5\lambda$, before decreasing and then remaining constant at -4.5dB. The peak amplitude occurs at the largest L where the incident field from the target sums entirely constructively. As L increases beyond this limit, destructive interference between the true peak and the previously-mentioned artefact occurs, reducing overall amplitude of the true peak before entering a final regime where the true peak and artefact are completely separated and the amplitude of the larger true peak remains constant.

In a 2D simulation, the peak amplitude of the PSF and PSF Area are inversely related and provide the same quantitative information on focusing and imaging performance [1-2] but it is clear from Fig. 4 that this is not the case for the 3D model. The appearance of the second "artefact signal" from the point target (a direct result of the finite length of the elements) causes the conventional measurement of the PSF area of a 2D image to vary depending on XdB threshold applied and therefore does not constitute a reliable metric to measure 2D imaging performance of a linear array simulated in 3D. Additionally, the PSF area is defined for each image separately and so contains no added information regarding absolute sensitivity as a function of element length that is contained in Fig. 4(b) and is therefore given no further consideration in this work.

Noise Spread Function & Simulated SNR

Analyzing the behavior of the PSF provides an insight into how element length (L) influences fundamental imaging capability. The main observations being a reduced sensitivity for lower values of L followed by a clear peak in the PSF amplitude culminating with the appearance of a secondary artefact signal as L increases further. What is not clear from analysis of the image due to a single point target is how element length affects the level of noise observed in an image obtained from a material with a high level of microstructural noise. From inspection of (4) it is clear that this information is contained in an integral over the PSF's from all positions in the material volume. To investigate this integral the Noise Spread Function (NSF) is introduced. The NSF is defined as $P(\boldsymbol{q} \mid \boldsymbol{r})$ and describes the contribution to backscatter from the position $\boldsymbol{q}$ to a single given image position $\boldsymbol{r}$ (this is complementary to the PSF which describes the image as a function of $\boldsymbol{r}$, given the position of single scatterer at $\boldsymbol{q}$). Figure 5(a-c) shows example renderings of the NSF for $\boldsymbol{r} = [0, 0, 10\lambda]$ for an L of 1λ, 5λ and 10λ respectively.

To visualize the NSF, an isosurface is used that encloses all points that are of amplitude greater than -20 dB relative to the maximum amplitude of the function. This surface shows the positions of grains that provide the main contribution to image noise at the given position $\boldsymbol{r}$. The volume contained within this isosurface can be used as a scalar metric to quantify the NSF. The NSF is a useful tool for visualizing noise contribution in a material with Fig. 5(a) showing an NSF volume of $40.2\lambda^3$ and the shape of -20 dB isosurface describing an arc of radius $|\boldsymbol{r}|$ about the center of the elements. For $L=5\lambda$, Fig. 5 shows the NSF volume decreases to $12.3\lambda^3$ with the -20 dB isosurface now localized at the imaging point. For $L=10\lambda$, the NSF volume increases again to $38.5\lambda^3$ with the -20 dB isosurface now centered along a straight line parallel to the y-axis through the imaging position.

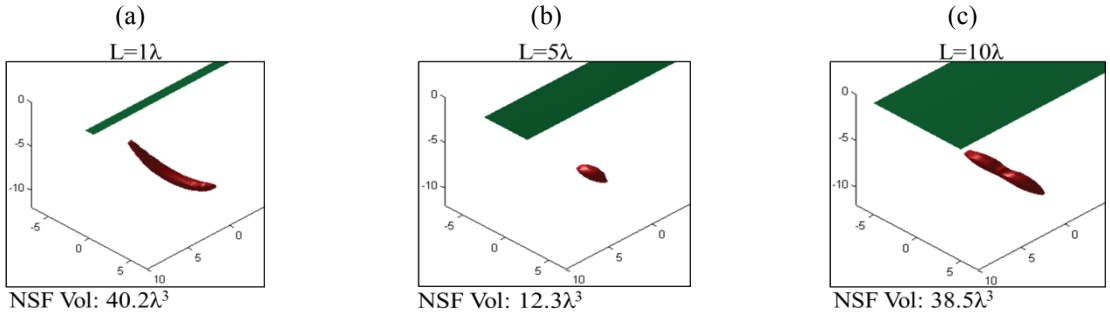

FIGURE 5. -20dB isosurface renderings of the Noise Spread Function (NSF) for an image point at a depth of 10λ directly below the array. The NSF volume describes the main contribution to backscatter at a given image position. (a) *L=1λ,* (b) *L=5λ*, (c) *L=10λ*.

The shape of the NSF in the material with L is related to divergence or directivity of the ultrasonic beam perpendicular to the focusing plane at the given imaging position but the NSF alone does not clearly provide any additional information about relative noise amplitude or SNR behavior. Figure 6 and Fig. 7 show the peak PSF amplitude or "signal" and image noise measurements (image noise amplitude and the NSF volume) and combines them to deduce a SNR as a function of L evaluated at [0, 0, 5λ] and [0, 0, 15λ] respectively. The simulated array consisted of 30 elements of $W=0.5\lambda$ emitting a normalized frequency spectrum with a fractional -20dB bandwidth of 100%, the inter-element spacing of the array is assumed negligible so that $P=W$. It is important to note in these results the SNR is relative not absolute.

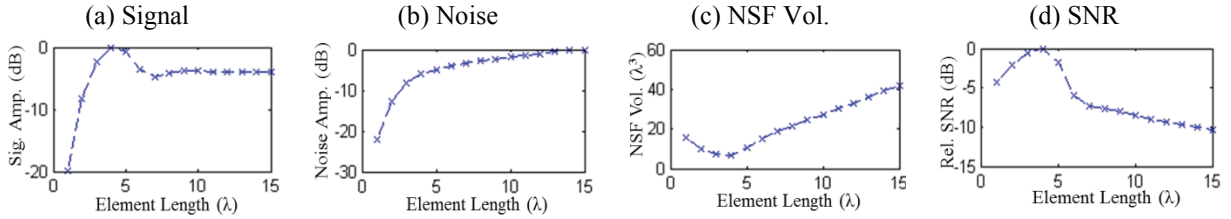

FIGURE 6. Signal and noise characteristics as a function of L for a point target at a depth 5λ directly below the array. (a) Signal amplitude, (b) Noise Amplitude, (c) NSF volume evaluated at the target position and (d) Relative SNR of the point target.

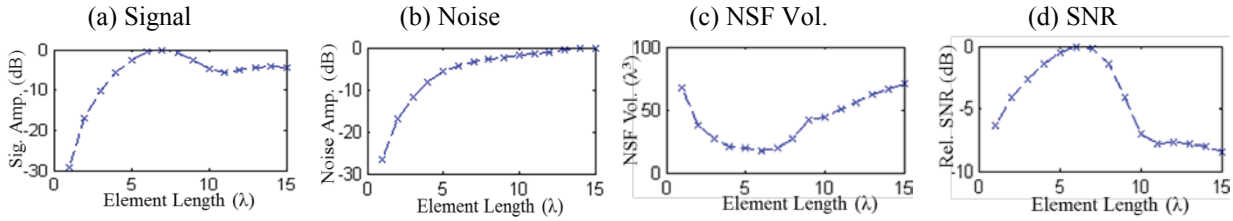

FIGURE 7. Signal and noise characteristics as a function of L for a point target at a depth 15λ directly below the array. (a) Signal amplitude, (b) Noise Amplitude, (c) NSF volume evaluated at the target position and (d) Relative SNR of the point target.

A single peak in the relative SNR plots is evident in both figures after which the SNR decreases monotonically corresponding to a regime where the signal remains constant with L and the image noise amplitude increases. A reduction from the optimal SNR of up to 11dB is shown for the range of L considered. This is a significant factor in imaging capability especially in noisy materials and high frequency applications. The position of the optimal SNR depends on the target depth and is shown to increase from *L=4* to *L=6* for target positions of [0, 0, 5λ] and [0, 0, 15λ] respectively. In both figures the maximum SNR occurs at the value of L where the PSF peak amplitude is maximized and the NSF volume is minimized. This was observed for all other target depths modelled in this work and suggests that the NSF volume and PSF amplitude are inversely related. An important practical consequence of this result implies that the optimal element length for a given image position can be determined entirely from the PSF of a target

at that image position. This negates the need for a time consuming 3D noise simulation that requires the calculation of the contributions of each grain or target position to image noise.

Beam Profile

Figure 6 and Fig. 7 demonstrate that the optimal array element length, $L_{Opt}(\boldsymbol{r})$ (or more specifically, $L_{Opt}([0, 0, z])$), can be predicted directly from the PSF, without the need to simulate ultrasonic noise but $L_{Opt}(\boldsymbol{r})$ can also be related to the transmitted ultrasonic beam in the material in the *yz* plane, often termed the "beam profile" emitted from each element. Figure 8(a) shows a 2D representation of the emitted beam pressure for an $L=9\lambda$ element in *yz* plane of the 3D coordinate system with a plot of the on-axis pressure at $y=0$ shown in Fig. 8(b). The white and black dashed lines respectively indicate the depth of the maximum pressure amplitude (termed here the "Near-Field Depth") of the ultrasonic beam which can be used to define a transition point from the near-field regime to the far-field regime of the element. Figure 8(c) shows the Near-Field Depth position predicted for each *L* obtained from the 2D beam model compared with the $L_{Opt}(\boldsymbol{r})$ predicted from the PSF and SNR simulations. The dashed lines indicate $L=9\lambda$ that is also shown in Fig. 8(a) and Fig. 8(b). The correlation between the two plots is clearly visible demonstrating that $L_{Opt}(\boldsymbol{r})$ is the element length at which the Near-Field Depth occurs at the same point as the target depth.

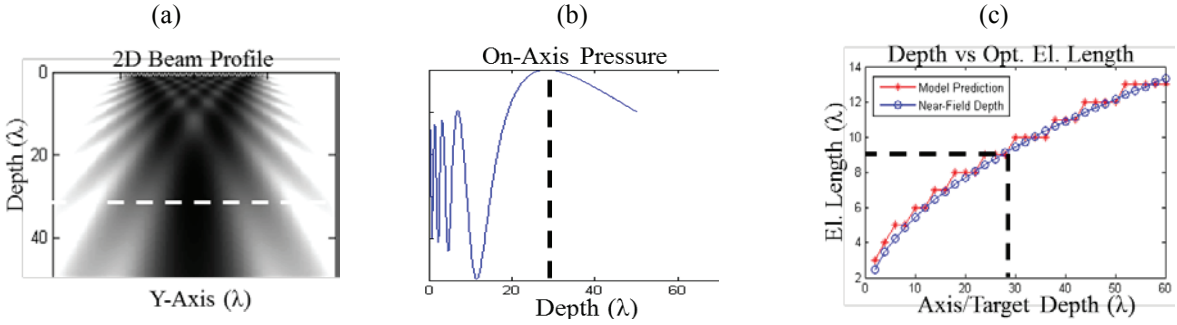

FIGURE 8. Relating the $L_{Opt}(\boldsymbol{r})$ to the natural focal point of the array. (a) 2D beam profile in YZ plane of an L=9λ element. (b) On-axis field pressure(y=0) of same *L* as a function of depth (*z*). (c) Peak on-axis pressure depth as a function of element length compared with predicted results for the $L_{Opt}(\boldsymbol{r})$ obtained from the 3D model SNR.

The Near-Field Depth is a good measure of the natural focal point of the elements in the *yz* plane and so it can be said that $L_{Opt}(\boldsymbol{r})$ is directly related to the natural focal spot of the array. It could be argued that this result is relatively obvious in a noise-free environment (as simulated by the 2D beam profile) it is not necessarily clear that this result extends to a more general array inspection including the effects of grain noise. This result shows that $L_{Opt}(\boldsymbol{r})$ can be predicted from a 2D beam model of the elements in the *yz* plane of the inspection geometry and so that $L_{Opt}(\boldsymbol{r})$ is independent of element pitch, width, or the number of elements. The direct relation to the ultrasonic beam profile additionally suggests validity of this observation holds for more practical wedge or immersion array inspection applications.

Array Design Guidelines

The work so far has demonstrated that $L_{Opt}(\boldsymbol{r})$ for a point-like scatterer can be determined by maximizing the PSF over *L* as well as directly from a 2D beam profile perpendicular to the imaging plane. This is a significant result from a general array optimization perspective but potentially of more importance from an industrial standpoint is to understand the approximate SNR "penalty" to be expected when using an array with non-optimal element length. Typically an industrial NDT group uses a set of ultrasonic arrays that are applied to a large variety of different inspections and it is not cost-effective to have bespoke arrays for every individual inspection. In order to understand this problem a return to the full 3D noise model SNR predictions is required as shown in Fig. 9(a) for target depths of 5λ, 10λ and 15λ. The Relative SNR values are plotted as a function of the normalized element length (L/L_{Opt}) for each target depth. All 3 curves show the same dependence on L/L_{Opt} suggesting that some general guidelines can be devised applicable for target depths and element lengths. The relative SNR behavior can be approximately split into three regions with reference to equation (4) as well as the individual signal and noise components of the Relative SNR shown in Fig. 6 and Fig. 7.

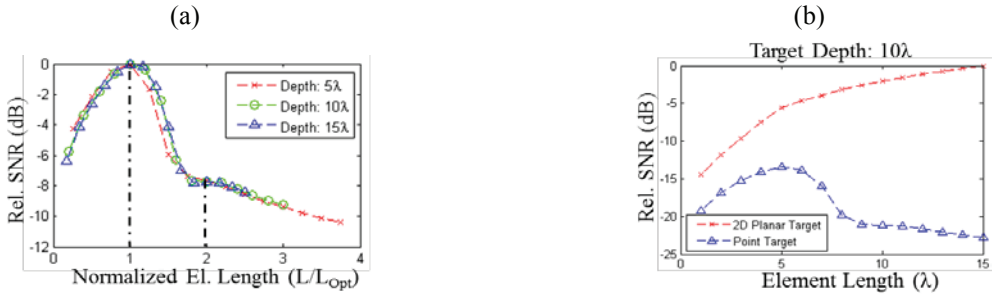

FIGURE 9. Relative SNR plots describing guidelines for understanding the effect of element on length on volumetric flaw detectability. (a) SNR as a function of element length normalized to L/L_{Opt}. (b) Relative SNR of volumetric target compared to 2D target.

In the first region, $0< L/L_{Opt}<1$ the signal from the target is increasing at a faster rate than the noise with SNR improving by a maximum of 7dB. For $1\leq L/L_{Opt}<2$ the signal amplitude decreases by -4.5dB (Fig. 6(a)) due to destructive interference across the element aperture which combined with the consistent increase in noise amplitude results in a sharp decrease in SNR of -8dB over the region. In the final region, $L/L_{Opt} \geq 2$, the signal from the point target remains constant and noise increases at a rate proportional to $L^{0.5}$ corresponding to an additional -1.6dB SNR reduction per L/L_{Opt} or alternatively -0.6dB per λ in addition to the -8dB reduction.

It is instructive to compare the relative SNR of a point target to that of a 2D planar specular target (infinite in the y-direction) the results of which are shown in Fig. 9(b). This provides a useful analytical comparison of linear array performance between a volumetric flaw and a 2D "long" crack-like flaw. The relative SNR of the 2D reflector is always larger than that of the point target because of reduced levels of beam spread from a specular target with a consistent rise in SNR because the received signal increases linearly with L. The rise in 2D SNR means that there is no "one size fits all" approach to optimizing L to suit both 2D and 3D reflectors.

In the context of this paper small volumetric flaws were defined as flaws that scatter ultrasound in a similar way to a point target; these include defects such as gas pores, inclusions and tip signals from short through-wall cracks but the validity of this assumption is closely the related to the size of the flaws relative to λ in addition to the distance of the flaw to the array aperture. The behavior of a flaw with finite but significant extent in the y-direction will have a relative SNR curve with characteristics in between the two extremes in Fig. 9(b). For small elements the behavior will be similar to a 2D scatterer; as L increases it will reach a peak SNR which would occur at a larger L than the point target, followed by a steady decline as predicted by Fig. 9(a). It is also important to consider the simplifications made in the noise model. For coarse grained materials or austenitic welds of comparable y-axis grain size to λ then the assumption of no spatial correlation of grain scattering breaks down and the behavior of the SNR predicted by this simplified noise model may differ slightly. It should also be noted that this work is frequency independent and does not consider any improvement of lowering the probe frequency on absolute SNR performance in noisy materials. With these considerations in mind the choice of element length (at a given probe frequency) should ultimately be based on the defect detection requirements for 2D and 3D defects which is specific to the inspection standard that is required to be achieved. For challenging coarse grained materials and components where pores and small inclusions are not permitted it may be beneficial to choose L close to the $L_{Opt}(\boldsymbol{r})$ to maximize the probability of detection.

CONCLUSIONS

An optimization study has been presented investigating the effect of element length on the imaging of volumetric defects using linear ultrasonic arrays. An analytical 3D ultrasonic simulation was used to determine the relative SNR of a point target at different positions in a material with a significant (12dB) change in SNR predicted over the range of element lengths and target depths considered; this demonstrates the importance of this parameter. In the analysis of the SNR the individual outputs of the simulation were considered in turn and the Noise Spread Function (NSF) of the imaging system was introduced to visualize the contribution to backscatter from each material grain at a given image point. It was then shown that the optimal element length can be predicted entirely from the Point Spread Function (PSF) of the system as well as the natural focal point of the elements perpendicular to imaging plane. An important consequence of these results suggests that a 3D grain noise simulation is not required to predict the optimal element

length, thus reducing the computational burden significantly. Practical guidelines for optimizing element length are then obtained directly from the SNR results at different target depths.

ACKNOWLEDGMENTS

This work was supported by BAE Systems Submarines and the UK Engineering and Physical Sciences Research Council through the UK Research Centre in NDE (RCNDE).

REFERENCES

1. C. Holmes, B. W. Drinkwater and P. D. Wilcox, *NDT&E Intl.,* **38**, 701-711 (2005).
2. P. D. Wilcox, "Ultrasonic Arrays in NDE: Beyond the B-Scan", in *Review of Progress in Quantitative Nondestructive Evaluation,* eds. D. O. Thompson and D. E. Chimenti, (American Institute of Physics 1511, Melville, NY) **32**, 33-50 (2013).
3. P. D. Wilcox, "Optimization of Array Element Pitch for NDE Applications", in *Review of Progress in Quantitative Nondestructive Evaluation,* eds. D. E. Chimenti and L. J. Bond, (American Institute of Physics 1650, Melville, NY) **34**, 952-961 (2015).
4. A. Van Pamel, M. J. S. Lowe, C. R. Brett, *IEEE Trans. UFFC*, **61**(12), 2042-2053 (2014).
5. Y. Humeida, P. D. Wilcox, M. D. Todd, B. W. Drinkwater, *NDT & E Intl*., **68**, 43-52 (2014).
6. F. J. Margetan, R. B. Thompson , and I. Yaldamooshadbad, "Modeling Ultrasonic Microstructural Noise in Titanium Alloys", in *Review of Progress in Quantitative Nondestructive Evaluation*, eds. D. O. Thompson and D. E. Chimenti, (Plenum Press, New York, NY) **12**, 1735-1742 (1993).
7. P. D. Wilcox, "Array Imaging of Noisy Materials", in *Review of Progress in Quantitative Nondestructive Evaluation,* eds. D. O. Thompson and D. E. Chimenti, (American Institute of Physics 1335, Melville, NY) **30**, 890-897 (2011).
8. T. S. Barber, P. D. Wilcox, and A. D. Nixon, "A Comparison of 1D and 1.5D Arrays for Imaging Volumetric Flaws in Small Bore Pipework", in *Review of Progress in Quantitative Nondestructive Evaluation,* eds. D. O. Thompson and D. E. Chimenti, (American Institute of Physics 1511, Melville, NY), **34**, 962-969 (2015).